



Machine learning modeling of lung mechanics: Assessing the variability and propagation of uncertainty in respiratory-system compliance and airway resistance



José Barahona ^{a,b}, Francisco Sahli Costabal ^{b,c}, Daniel E. Hurtado ^{a,b,d,*}

^a Department of Structural and Geotechnical Engineering, School of Engineering, Pontificia Universidad Católica de Chile, Santiago, 7820436, Chile

^b Institute for Biological and Medical Engineering, Schools of Engineering, Medicine and Biological Sciences, Pontificia Universidad Católica de Chile, Santiago, 7820436, Chile

^c Department of Mechanical and Metallurgical Engineering, School of Engineering, Pontificia Universidad Católica de Chile, Santiago, 7820436, Chile

^d Institute for Medical Engineering and Science, Massachusetts Institute of Technology, Cambridge, MA, 02140, USA

ARTICLE INFO

Keywords:

Lung modeling
Respiratory mechanics
Machine learning
Multi-fidelity Gaussian process
Sensitivity analysis
Uncertainty quantification

ABSTRACT

Background and Objective: Traditional assessment of patient response in mechanical ventilation relies on respiratory-system compliance and airway resistance. Clinical evidence has shown high variability in these parameters, highlighting the difficulty of predicting them before the start of ventilation therapy. This motivates the creation of computational models that can connect structural and tissue features with lung mechanics. In this work, we leverage machine learning (ML) techniques to construct predictive lung function models informed by non-linear finite element simulations, and use them to investigate the propagation of uncertainty in the lung mechanical response.

Methods: We revisit a continuum poromechanical formulation of the lungs suitable for determining patient response. Based on this framework, we create high-fidelity finite element models of human lungs from medical images. We also develop a low-fidelity model based on an idealized sphere geometry. We then use these models to train and validate three ML architectures: single-fidelity and multi-fidelity Gaussian process regression, and artificial neural networks. We use the best predictive ML model to further study the sensitivity of lung response to variations in tissue structural parameters and boundary conditions via sensitivity analysis and forward uncertainty quantification. Codes are available for download at <https://github.com/comp-medicine-uc/ML-lung-mechanics-UQ>

Results: The low-fidelity model delivers a lung response very close to that predicted by high-fidelity simulations and at a fraction of the computational time. Regarding the trained ML models, the multi-fidelity GP model consistently delivers better accuracy than the single-fidelity GP and neural network models in estimating respiratory-system compliance and resistance ($R^2 \sim 0.99$). In terms of computational efficiency, our ML model delivers a massive speed-up of $\sim 970,000\times$ with respect to high-fidelity simulations. Regarding lung function, we observed an almost matched and non-linear behavior between specific structural parameters and chest wall stiffness with compliance. Also, we observed a strong modulation of airways resistance with tissue permeability.

Conclusions: Our findings unveil the relevance of specific lung tissue parameters and boundary conditions in the respiratory-system response. Furthermore, we highlight the advantages of adopting a multi-fidelity ML approach that combines data from different levels to yield accurate and efficient estimates of clinical mechanical markers. We envision that the methods presented here can open the way to the development of predictive ML models of the lung response that can inform clinical decisions.

* Corresponding author at: Department of Structural and Geotechnical Engineering, School of Engineering, Pontificia Universidad Católica de Chile, Santiago, 7820436, Chile.

E-mail address: daniel.hurtado@uc.cl (D.E. Hurtado).

1. Introduction

Mechanical ventilation (MV) is a life-saving treatment for patients under respiratory failure who are unable to spontaneously perform gas exchange [1]. MV was crucial during the recent COVID-19 pandemic, which has affected more than 670 million people worldwide [2], where many of those hospitalized have received ventilatory support in intensive care units [3,4]. One of the challenges in the management of patients connected to MV is to titrate the ventilator settings in a personalized and optimal way. To this end, two key physiological parameters traditionally assessed during MV therapy are *airways resistance* and *respiratory-system compliance*, which describe the respiratory mechanics of a patient. Airways resistance measures the opposition to airflow in the airways given a certain pressure difference. Respiratory-system compliance measures the ability of the coupled lung and rib cage system to expand. Clinical evidence has shown that these parameters display high variability and heterogeneity among patients who develop acute respiratory distress syndrome [5–7]. Recently, lung computational models that are built from medical images using a continuum poromechanical framework [8–10] have shown to capture the behavior of lungs connected to MV, predicting respiratory mechanics parameters that fall within the range observed in clinical settings [11].

One salient feature of Machine Learning (ML) methods is the acceleration of complex biomedical simulations. Some recent notable examples are found in cardiovascular simulations [12], where ML models have been explored to study the multiscale function of failing hearts [13], to predict activation mappings based on cardiac electrophysiology simulations [14], and to determine the structural stress tensor and blood velocity field in coronary arteries [15,16]. Other novel applications are found in biological systems, where ML has been used to create reduced-order surrogate models in predicting the skin behavior during reconstructive surgery [17], and simulating the mechanical behavior of human livers in real time [18]. In the context of respiratory medicine, ML techniques have been explored in the analysis of medical images, with successful applications in image segmentation of lungs and respiratory structures [19,20], disease diagnosis using image-based features [21,22], and in the estimation of MV parameters via inverse mapping [23]. However, to the best of our knowledge, the development of ML models for predicting respiratory mechanics parameters in human lungs remains an open avenue of research.

A compelling application of biomechanical simulations is the study of the variability and uncertainty that arises in biological systems via sensitivity analysis (SA) and uncertainty quantification (UQ). SA and UQ provide a rigorous framework to determine the importance of input variables and the effect of uncertainty propagation. Since these tasks are usually challenging due to the large number of required evaluations, coupling high-fidelity biomechanical models with ML or similar frameworks has proved to be a powerful tool. In this regard, we can find crucial contributions in the study of the response of electromechanical cardiac models and ventricular function via polynomial chaos expansion (PCE) [24,25], in the implementation of Gaussian processes (GPs) emulators to perform global sensitivity analysis in multi-scale and fluid dynamics heart models [26,27], and uncertainty quantification tasks on insulin and in-stent restenosis models [28,29], among others. Given that high-fidelity data could be difficult to obtain due to the elevated experimental and computational cost associated, an appealing option when building predictive models of biological function is to leverage multi-fidelity approaches that combine reliable data (expensive) with different levels of low-fidelity data (less expensive). We can find related works in the implementation of multi-fidelity GPs to study the effect of drugs on the QT interval in electrophysiological models [30], quantifying the importance of structural and mechanical parameters in tissue growth dynamics [31,32], and assessing inducible regions of atrial fibrillation models [33], among others. In the same context, recent contributions have implemented multi-fidelity approaches via artificial neural networks (ANNs) architectures for uncertainty quantification tasks in

biological and physical systems [34–36]. Regarding lung system, the application of SA and UQ techniques to understand how tissue structural properties impact respiratory mechanics using lung simulations has been less studied and remains an open avenue of research.

In this work, we explore ML techniques in the construction of predictive lung function models that are informed by nonlinear finite element (FE) simulations. We further use these ML models to study the sensitivity of lung mechanics to variations in tissue structural parameters and boundary conditions. In addition, we assess how uncertainty in these input parameters propagates through the lung model. To this end, in Section 2 we revisit a continuum poromechanical formulation of the lungs suitable for determining respiratory-system compliance and airway resistance. Based on this framework, we create high-fidelity non-linear FE models of the lungs from medical images. Given the high computational cost of such models, we develop and validate a low-fidelity lung model based on an idealized thick-wall sphere geometry. We then study the application of three ML architectures: single-fidelity and multi-fidelity Gaussian process regression, and neural networks. In section 3, we use high-fidelity and low-fidelity simulations to train and test the performance of ML models in predicting lung mechanics parameters. Using the best ML model, we perform SA and forward UQ to assess parameter sensitivity and construct probability distributions of compliance and resistance that result from assuming varying levels of dispersion in the input parameters. We end in Section 4 by discussing the advantages of a multi-fidelity framework in modeling lung mechanics, the relevance of certain constitutive parameters and boundary conditions in the respiratory-system response, as well as offering a perspective of future work that stems from our findings.

2. Methods

Codes are available for download at <https://github.com/comp-medicine-uc/ML-lung-mechanics-UQ>

2.1. Continuum poromechanical framework for lung modeling

In the following, we adopt the poromechanical formulation introduced in [11] for the creation of FE models of lungs assisted with MV. This framework considers the air-tissue mechanical interaction in the lung parenchyma and models airflow in the lung as a porous flow in a continuum. Let Ω_0 be the lung domain in the reference (end-of-expiration) configuration, and $\Omega = \varphi(\Omega_0, t)$ be its deformed configuration at time instant t , where φ is the deformation mapping that connects these two states. We define the deformation gradient as $F = \nabla\varphi(X, t)$ and the volumetric change by its determinant $J = \det(F)$. To characterize airflow, we denote by P_{alv} the alveolar pressure field in the lung defined in the reference configuration. Let Γ_0 be the boundary of the reference configuration Ω_0 . We assume it admits the partition $\Gamma_0 = \Gamma_\varphi \cup \Gamma_T$ with $\Gamma_\varphi \cap \Gamma_T = \emptyset$, $\Gamma_P \cup \Gamma_Q = \Gamma_0$ and $\Gamma_P \cap \Gamma_Q = \emptyset$, where Γ_φ , Γ_T , Γ_P and Γ_Q are the boundaries of prescribed displacement, tractions, pressures, and alveolar flow, respectively. With these fields and boundaries definitions, the strong formulation of the lung poroelastic model can be stated as

Find $\varphi \in C^2(\Omega_0 \times [0, T], \mathbb{R}^N)$ and $P_{alv} \in C^2(\Omega_0 \times [0, T], \mathbb{R})$ such as:

$$\operatorname{Div}(P) + RB = 0, \quad \text{in } \Omega_0 \times (0, T), \quad (1)$$

$$\frac{\partial J}{\partial t} + \operatorname{Div}(Q) = 0, \quad \text{in } \Omega_0 \times (0, T), \quad (2)$$

$$\varphi = \varphi_0, \quad \text{in } \Omega_0, \quad (3)$$

$$P_{alv} = P_0, \quad \text{in } \Omega_0, \quad (4)$$

$$\varphi = \bar{\varphi}, \quad \text{on } \Gamma_\varphi \times (0, T], \quad (5)$$

$$P \cdot N = \bar{T}, \quad \text{on } \Gamma_T \times (0, T], \quad (6)$$

$$P_{alv} = \bar{P}, \quad \text{on } \Gamma_P \times (0, T], \quad (7)$$

$$Q \cdot N = \bar{Q}, \quad \text{on } \Gamma_Q \times (0, T], \quad (8)$$

where Eq. (1) and (2) correspond to the material form of the linear momentum conservation for the tissue and the mass conservation equation of the gas, respectively. The field \mathbf{P} represents the first Piola-Kirchhoff stress tensor, and is related to the deformation mapping and alveolar-pressure fields by $\mathbf{P} = \mathbf{P}' - J P_{alv} \mathbf{F}^{-T}$, where $\mathbf{P}' = \partial W / \partial \mathbf{F}$ is the constitutive relation of the lung parenchyma with W as the strain energy function that characterizes the hyperelastic behavior of alveolar tissue in the parenchyma. Further, \mathbf{Q} corresponds to the material airflow field, and is related to the primary fields through Darcy's law, which takes the form $\mathbf{Q} = \frac{1}{\eta} \mathbf{J} \mathbf{F}^{-1} \boldsymbol{\kappa} \mathbf{F}^{-T} [-\text{grad}(P_{alv}) + \rho_a \mathbf{F}^T \bar{\mathbf{B}}]$, with $\boldsymbol{\kappa} = \kappa \mathbf{I}$ is the intrinsic permeability tensor for an isotropic medium, with a permeability term defined as $k = \kappa / \eta$. The term $\bar{\mathbf{B}}$ corresponds to the material field of body forces, which in this study we set to zero, neglecting the effect of gravity. In addition, $\varphi_0 : \Omega_0 \rightarrow \mathbb{R}^3$ and $P_0 : \Omega_0 \rightarrow \mathbb{R}$ are the initial values of the deformation and alveolar pressure fields, and $\bar{\varphi}$, \bar{T} , \bar{P} , \bar{Q} are the prescribed deformations, tractions, alveolar pressure, and alveolar flow, respectively.

In our study, we represent the mechanical behavior of alveolar tissue by the nonlinear hyperelastic model developed in [37], which yields a mechanical response with pulmonary compliance values that are in the range of those reported for normal human lungs [11]. The associated strain energy function is given by

$$W(\mathbf{C}) = c(I_1(\mathbf{C}) - 3) + \frac{c}{\beta}(I_3(\mathbf{C})^{-\beta} - 1) + c_1(I_1(\mathbf{C}) I_3(\mathbf{C})^{-1/3} - 3)^{d_1} + c_3(I_3(\mathbf{C})^{1/3} - 1)^{d_3}, \quad (9)$$

where \mathbf{C} is the right Cauchy-Green tensor, and $I_1(\mathbf{C})$, $I_3(\mathbf{C})$ are the corresponding invariants of \mathbf{C} . The baseline values of the constitutive model parameters are

$$c = 0.3567 \text{ kPa}, \quad \beta = 1.075, \quad c_1 = 0.2782 \text{ kPa}, \quad c_3 = 5.766 \cdot 10^{-3} \text{ kPa}, \\ d_1 = 3, \quad d_3 = 6, \quad (10)$$

which modulate the volumetric and isochoric components of the mechanical response. In particular, c and β are related to the Young's modulus E and Poisson's ratio ν by $E = 4c(1 + \nu)$ and $\nu = \beta/(1 + 2\beta)$, respectively. All parameters are calibrated from experimental data obtained in pressure-volume-change experiments and uniaxial tensile tests of lung strips. The exponents d_1 and d_3 were set to integer positive values that comply with growth and positiveness restrictions for strain energy functions. In this work, we are interested in studying how uncertainty in the constitutive parameters c , β , c_1 , and c_3 affects the lung response, while d_1 and d_3 are kept fixed.

2.2. High-fidelity lung model

Using the poromechanical formulation described above, we construct high-fidelity FE models of human lungs. The anatomical domain is extracted from computed tomography (CT) images of human subjects previously reported in the literature [38], see Fig. 1a. From these images, we construct tetrahedral discretizations following the procedures detailed in [39], which results in tetrahedral meshes with 59,355 elements for the right lung and 45,288 elements for the left lung, see (Fig. 1b). We divide the model domain into two boundaries: the airway surface and the visceral pleural surface overlying the remaining lung surface. With this, we consider a boundary condition representative of the inflation-deflation process: to represent the application of pressure-controlled MV, the air is supplied by a prescribed pressure \bar{P} at the airway boundary, denoted Γ_{aw} . To model the interaction of the lung with the ribcage, we consider spring elements with stiffness coefficient K_s , which represent a Robin condition of the form $\bar{T}(\mathbf{X}) = K_s \{\varphi(\mathbf{X}) - \mathbf{X}\}$. As baseline values, we consider an isotropic permeability of $k = 10^4 \text{ mm}^2/\text{kPa}\cdot\text{s}$ and a spring stiffness coefficient of $K_s = 80 \cdot 10^{-3} \text{ kPa/mm}$, which were previously adjusted to provide a physiological response. In addition to the parameters selected for the constitutive tissue model,

we are interested in studying the sensitivity of the lung model to uncertainties in k and K_s , as they control the airflow in parenchymal tissue and the elastic response of the ribcage, respectively.

For the spatiotemporal discretization of the poroelastic formulation, we use a backward-Euler time-integration scheme and a standard Galerkin FE discretization. We implement the numerical scheme in the FEniCS library [40], using Python 3.8. It is important to note that for high-fidelity simulations, we replace the left lung with a mirror of the right lung in order to have a symmetrical domain of both lungs and, therefore a fair comparison with the simulations of the low-fidelity model we describe next.

2.3. Low-fidelity lung model

With the aim of reducing the computational burden, we develop a low-fidelity FE lung model based on a simplified geometry. For this purpose, we replace the lung domain by a homogeneous hollow sphere, which, using symmetry consideration, we model using only one-eighth of the volume, see Fig. 1c. The outer surface represents the visceral pleura, and the inner surface corresponds to the airways cross section. The boundary conditions on the remaining surfaces are set such that $\mathbf{u} \cdot \mathbf{N} = 0$, which are justified by the symmetry of the model. The dimensions of the low-fidelity model are defined such that the domain volume and inner surface are roughly the same as the lungs volume and airway inlet cross-section, respectively. For the generation of the tetrahedral mesh we use the open-source tetrahedral mesh generator Gmsh [41], which delivers a mesh with 2,665 tetrahedral elements and 370 nodes.

2.4. Simulation of lung mechanics and determination of respiratory-system compliance and resistance

We use the lung FE models defined in previous sections to simulate their response during MV in a pressure-controlled mode [42]. In this setting, the airway pressure is prescribed by the ventilator, and the lung response is typically monitored in terms of lung volume and airway flow signals. To simulate this setting, we consider time-dependent pressure boundary conditions at the airway cross section that resemble the MV square-wave pressure signals used in clinical settings, which are represented by a function $\bar{P}(t)$ [43]. At the onset of inspiration, this function increases linearly until the peak inspiratory pressure (PIP), such that $\bar{P} = \text{PIP}$ is reached and maintained, which, in order to deliver a physiological response, is set at 6 cm H₂O [11]. Then, the pressure returns to zero during the expiratory phase ($\bar{P} = 0$), after which another respiratory cycle is repeated. To simulate a normal lung at rest, each cycle considers 1 second of inspiration followed by 2 seconds of expiration, equivalent to a respiratory rate of 20 breaths per minute [44].

Once the FE lung simulations are performed, we compute the tidal volume signal, flow signal, and airways pressure signal as

$$V_{\text{sim}}(t) := \int_{\Omega_0} J d\Omega_0 - V_{\text{lung},0}, \quad (11)$$

$$\dot{V}_{\text{sim}}(t) = \frac{\partial V_{\text{sim}}}{\partial t}, \quad (12)$$

$$P_{\text{aw,sim}}(t) := \bar{P}(t). \quad (13)$$

The breathing process is highly dependent on the compliance of the respiratory system C_{rs} and the airways resistance R [45], both parameters of clinical relevance. Respiratory-system compliance measures the ability of the coupled lung-rib cage system to stretch and expand under a given pressure level, thus, is an important indicator of lung health and function [43]. Airways resistance measures the degree of resistance to air flow through the respiratory tract during inspiration and expiration process. To compute these parameters from the pressure, volume and flow signals, we first consider the single-compartment equation of motion, which reads

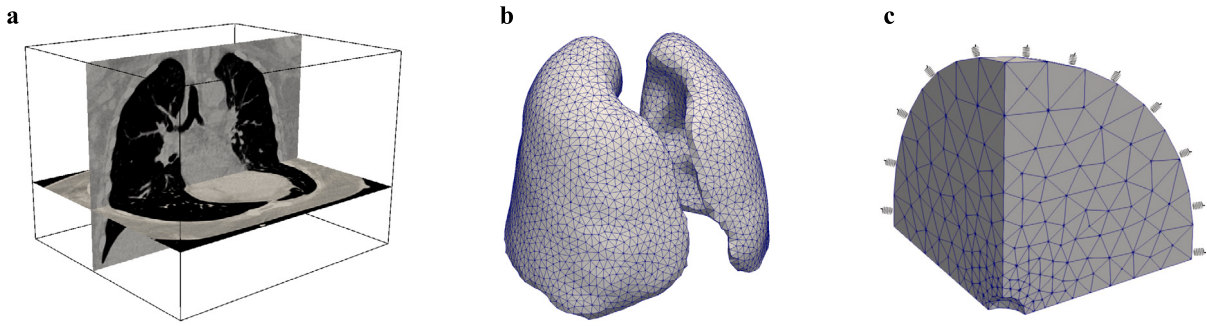


Fig. 1. Construction of high-fidelity and low-fidelity lung finite-element models. (a) Computed-tomography image from which the lung domain is determined, (b) high-fidelity finite-element mesh generated from image lung domain, and (c) finite-element mesh generated for the low-fidelity lung model.

$$P_{aw}(t) = \frac{V(t)}{C_{rs}} + R\dot{V}(t), \quad (14)$$

where P_{aw} is the pressure at the airways inlet, V is the lung volume, and \dot{V} is the airflow. Then, using the signals defined in (11), (12), and (13), which are constructed from the FE simulations, we consider the objective function

$$S = \sum_{t_i=0}^T [P_{aw,sim}(t_i) - \frac{V_{sim}(t_i)}{C_{rs}} + R\dot{V}_{sim}(t_i)]^2 \quad (15)$$

where t_i is a simulation time value between 0 and T (end of one respiratory cycle). This objective function can be minimized using a least-squares fitting approach, from which we can obtain the values of C_{rs} and R , see [11] for further details on this procedure. Both respiratory-system compliance and airways resistance are time-independent quantities of interest that modulate the dynamic response of the lung. We will be interested in studying how uncertainties in the constitutive parameters affect them.

2.5. Machine learning modeling: multi-fidelity Gaussian process regression and neural networks

Up to this point, we have a high-fidelity and low-fidelity model. However, assuming that both present a considerable cost in computational time, performing a large number of evaluations for our uncertainty quantification analysis may not be a feasible task. Therefore, we are interested in building a surrogate model which allows us to emulate the high-fidelity simulations but at a much lower computational cost. More specifically, through this surrogate, we want to predict the respiratory-system compliance C_{rs} or airway resistance R given a set of parameters of the lung model. For this purpose, our first choice to build this model is through a Gaussian Process (GP) [46], a Bayesian regression method that we train from data to predict an output, thus classifying it as a ML technique. Considering a general regression problem, we assume that we have a dataset of the form $\mathcal{D} = (\mathbf{X}, \mathbf{y})$, where $\mathbf{X} \in \mathbb{R}^{M \times d}$ is the collection of M observations of an input \mathbf{x} of dimension d , and $\mathbf{y} \in \mathbb{R}^M$ is the corresponding vector of outputs. With this consideration, we want to learn a latent function f from our dataset, such that $\mathbf{y} = f(\mathbf{X}) + \epsilon$, where ϵ is an independent, identically distributed (iid), Gaussian noise term with zero mean and unknown variance σ_G^2 to be learned from the data. First, we establish that our prior knowledge about f can be described by a GP with mean $m(\mathbf{x})$ and covariance $k(\mathbf{x}, \mathbf{x}'; \theta)$,

$$f(\mathbf{x}) \sim \mathcal{GP}(m(\mathbf{x}), k(\mathbf{x}, \mathbf{x}'; \theta)), \quad (16)$$

where we assume (without loss of generality) a zero-mean function $m(\mathbf{x}) = 0$. In our prior, θ denotes the hyperparameters of the covariance function or kernel, which encodes our assumption about the Gaussian process: when selecting a covariance function, we make implicit assumptions about the shape of the function we wish to encode with

the Gaussian process, e.g., how smooth it is [47]. Here, we choose a quadratic exponential kernel, expressed in the form

$$k(\mathbf{x}, \mathbf{x}'; \theta) = v \exp \left\{ - \sum_{i=1}^d \frac{(x_i - x'_i)^2}{2\ell_i^2} \right\}, \quad (17)$$

where v and $\{\ell_i\}_{i=1, \dots, d}$ are the model hyperparameters: v models the variance of the process, and ℓ_i determines the lengthscale of each input dimension. On the other hand, x_i and x'_i denote a pair of consecutive points in a dimension i . To adjust and find the optimal hyperparameters, we train the model by maximizing the log marginal likelihood function of the Gaussian process,

$$\log p(\mathbf{y} | \mathbf{X}, \theta) = -\frac{1}{2} \mathbf{y}^\top (\mathbf{K} + \sigma_G^2 \mathbf{I})^{-1} \mathbf{y} - \frac{1}{2} \log |\mathbf{K} + \sigma_G^2 \mathbf{I}| - \frac{M}{2} \log 2\pi, \quad (18)$$

where $\mathbf{K} \in \mathbb{R}^{M \times M}$ is a positive definite symmetric matrix: $K_{ij} = k(x_i, x_j, \theta)$ stores the covariance between each pair of points in \mathbf{x} . We can exemplify the effect of ℓ_i : short scales deliver low correlations in the covariance matrix, resulting in highly non-smooth functions, and long scales deliver highly correlated matrices, and hence, very smooth functions. The optimization of the likelihood function is performed with the L-BFGS method. After training the model, we compute the prediction of the posterior distribution at a new input location \mathbf{x}^* ,

$$p(\mathbf{y}^* | \mathbf{x}^*, \mathcal{D}) \sim \mathcal{N}(\mu(\mathbf{x}^*), \Sigma(\mathbf{x}^*)) \quad (19)$$

where

$$\mu(\mathbf{x}^*) = k(\mathbf{x}^*, \mathbf{X})(\mathbf{K} + \sigma_G^2)^{-1} \mathbf{x}, \quad (20)$$

and

$$\Sigma(\mathbf{x}^*) = k(\mathbf{x}^*, \mathbf{x}^*) - k(\mathbf{x}^*, \mathbf{X})(\mathbf{K} + \sigma_G^2)^{-1} k(\mathbf{X}, \mathbf{x}^*), \quad (21)$$

are the mean and the variance of the prediction, respectively.

The Gaussian Process regression model can be extended to leverage the availability of multifidelity data. To this end, we consider the observations coming from two levels: a high-fidelity dataset of the form $\mathcal{D}_H = (\mathbf{X}_H, \mathbf{y}_H)$, where $\mathbf{X}_H \in \mathbb{R}^{M_H \times d}$ is the collection M_H of an input \mathbf{x}_H with its corresponding output $\mathbf{y}_H \in \mathbb{R}^{M_H}$, and a low-fidelity dataset of the form $\mathcal{D}_L = (\mathbf{X}_L, \mathbf{y}_L)$, where $\mathbf{X}_L \in \mathbb{R}^{M_L \times d}$ is the collection M_L of an input \mathbf{x}_L and output $\mathbf{y}_L \in \mathbb{R}^{M_L}$. We leverage the fact that we can construct a higher number of low-fidelity data points with considerably less computational effort than high-fidelity data points, and therefore $M_L \gg M_H$. Thus, our goal is to systematically combine the low-fidelity (less accurate, less expensive) model observations with the high-fidelity ones (more accurate, more expensive), in order to predict the high-fidelity output more efficiently. With this consideration, we implement a multi-fidelity regression model, in which the high-fidelity function is modeled as the scaled sum of the low-fidelity function plus an error term [48],

$$f_H = f_{err}(\mathbf{x}) + \rho f_L(\mathbf{x}), \quad (22)$$

with

$$f_L(\mathbf{x}) \sim \mathcal{GP}(0, k_L(\mathbf{x}, \mathbf{x}'; \theta_L)), \quad (23)$$

and

$$f_{err}(\mathbf{x}) \sim \mathcal{GP}(0, k_H(\mathbf{x}, \mathbf{x}'; \theta_H)), \quad (24)$$

where $f_L(\mathbf{x})$ is a Gaussian process that models the outputs of the low-fidelity function, while ρ is a scaling factor indicating the correlation grade with the high-fidelity data (a value of $\rho = 0$ implies that there is no correlation between the low-fidelity and high-fidelity observations). At the same, $f_{err}(\mathbf{x})$ is also a Gaussian process that models the bias for the high-fidelity data. The above implies that the structure can be expressed as a single Gaussian process, with the following prior:

$$\mathbf{y} = \begin{bmatrix} \mathbf{y}_L \\ \mathbf{y}_H \end{bmatrix} \sim \mathcal{N}\left(\begin{bmatrix} \mathbf{0} \\ \mathbf{0} \end{bmatrix}, \begin{bmatrix} K_{LL} & K_{LH} \\ K'_{LH} & K_{HH} \end{bmatrix}\right), \quad (25)$$

where K_{LL} and K_{HH} model the correlation at each fidelity level, and K_{LH} models the correlation between low and high-fidelity levels.

Furthermore, we are interested in comparing the performance of the multi-fidelity surrogate with respect to other ML architectures considering only one level of fidelity. Thus, we additionally chose to build and train a single-fidelity GP-based model, and a single-fidelity neural network-based model, both trained with the high-fidelity data collection, M_H .

The single-fidelity GP model has already been described above, so it is naturally trained with the same configuration of high-fidelity data as the multi-fidelity GP model.

Regarding the neural network model, we want an approximation of the lung response of the form

$$\mathbf{y} \approx NN(\mathbf{x}, \theta_{NN}), \quad (26)$$

where \mathbf{x} is the already described vector of inputs, and NN is a neural network with architecture to be defined and parameters θ_{NN} , also called weights. Regarding the architecture, we consider a ReLU activation function between layers [49] and a linear activation function σ_L for the output of the last layer, thus our expected lung response reads as

$$\mathbf{y} \approx \sigma_L(NN(\mathbf{x}, \theta_{NN})). \quad (27)$$

To train the model and find the optimal weights in order to obtain a good approximation, we use the mean squared error loss function,

$$\mathcal{L}(\theta_{NN}) = \frac{1}{M_H} \sum_{i=1}^{M_H} (NN(\mathbf{x}_i) - \hat{y}_i)^2, \quad (28)$$

where $NN(\mathbf{x}_i)$ is the neural network prediction for an observation \mathbf{x}_i of the input, and \hat{y}_i is the corresponding output label. Then, to minimize the loss function we use the Adam optimizer [50], which is based on the stochastic gradient descent method. Moreover, to find the architecture with the best performance, we implement a grid search of the following hyperparameters: number of layers, neurons per layer, learning rate, and number of epochs.

2.6. Dataset creation and model training

With the previous methodology, we want to build an accurate ML surrogate model to predict the pulmonary response represented by the respiratory-system compliance C_{rs} and the airways resistance R . In this sense, and as already introduced, it is through this model that we also want to determine the variability of the response (output) with respect to the presence of uncertainty in some parameters of interest of the pulmonary model (inputs). These input parameters include those that determine the mechanical behavior of the lung tissue (c, β, c_1, c_3), those that modulate the airflow in the parenchyma (permeability k), and

Table 1

Input parameters for lung function model: baseline values and parameter ranges.

Parameter	Units	Baseline Value	Range
c	kPa	0.3567	[0.1784, 0.5351]
β	–	1.075	[0.5375, 1.6125]
c_1	kPa	0.2782	[0.1391, 0.4173]
c_3	kPa	$5.766 \cdot 10^3$	$[2.8830, 8.6490] \cdot 10^3$
k	$\text{mm}^2/\text{kPa} \cdot \text{s}$	$1 \cdot 10^4$	$[0.5, 1.5] \cdot 10^4$
K_s	kPa/mm	$80 \cdot 10^{-3}$	$[40, 120] \cdot 10^{-3}$

those that define the mechanical response of the chest wall (linear stiffness K_s). Regarding the range of values for each parameter, information on the variation of the lung tissue parameters among the different samples in the experimental tests is provided in [37]: with the exception of c_1 , the other parameters have a low variation, with c presenting a maximum one of approximately 15% between the lower/upper quartile and the median. On the other hand, as a physiological requirement, it is stated that all parameters must be positive. Under these considerations, we adopt a more conservative and general variation for all parameters, so we establish a maximum uncertainty range of $\pm 50\%$. The baseline values of each parameter and their maximum range are summarized in Table 1.

In order to build and train the multi-fidelity GP model, we obtain data sets from both fidelity levels. From the low-fidelity model, via Latin hypercube sampling, we sample and simulate $M_L = 200$ observations from the parameter space specified in Table 1, thus $\mathbf{X}_L \in \mathbb{R}^{200 \times 6}$ and $\mathbf{y}_L \in \mathbb{R}^{200 \times 2}$. Similarly, for the high-fidelity model we sample $M_H = 20$ observations, thus $\mathbf{X}_H \in \mathbb{R}^{20 \times 6}$ e $\mathbf{y}_H \in \mathbb{R}^{20 \times 2}$. To avoid large numerical differences between parameter values, we perform a standardization on the input data by subtracting the mean and dividing by the standard deviation each variable [51]. Regarding model training, for comparison purposes we split the high-fidelity data into a training and validation set, varying the size of the training set from 10 to 19 observations (i.e., using from 50% to 95% of the high-fidelity data for training). Additionally, we obtain a testing set by sampling 100 observations from both fidelity levels. To evaluate the accuracy of our surrogate model, we use a shuffle-split type cross-validation method with 10 repetitions, obtaining the mean root mean squared error (RMSE) on the testing set and its standard deviation. We construct and train our multi-fidelity surrogate model in Python using the open source library GPy [52] in conjunction with the Emukit toolbox [53].

For the single-fidelity GP model and the neural network, we perform the previous procedure in an analogous way, but as mentioned above, with the exception that only the high-fidelity data is available for training. Regarding the neural network architecture, we construct it using the open source library Tensorflow [54] and after training with 95% of the high-fidelity data, we determine an optimal architecture of 3 hidden layers with 60 neurons each, Adam optimizer, a learning rate of 0.1 and 10000 epochs.

It is important to note that we build separate ML surrogate models for the prediction of C_{rs} and R .

2.7. Sensitivity analysis

To analyze the sensitivity of the pulmonary response to the model parameters, we use a global method using Sobol indices [55], which allows us to quantify the impact of each parameter/variable on the response. We consider the output of our ML surrogate model $\mathbf{y} = f(\mathbf{X})$, where $\mathbf{X} \in \mathbb{R}^d$ is a vector of inputs with d parameters (x_1, \dots, x_d). According to this method, f and its variance can be decomposed as

$$\mathbf{y} = f_0 + \sum_{i=1}^d f_i(x_i) + \sum_{i<j}^d f_{ij}(x_i, x_j) + \dots + f_{1,2,\dots,d}(x_1, x_2, \dots, x_d),$$

$$Var(\mathbf{y}) = \sum_{i=1}^d V_i + \sum_{i<j}^d V_{ij} + \dots + V_{1,2,\dots,d}, \quad (29)$$

where f_0 is a constant term, f_i is a function of x_i , f_{ij} is a function of x_{ij} , and so on. A condition of this decomposition is that its terms are orthogonal to each other. Therefore, each component f_i can be interpreted as the effect on y due only to x_i . In turn, f_{ij} is interpreted as the effect on y when changing x_i and x_j simultaneously, with higher-order terms having analogous interpretations. Similarly, in variance-based decomposition, each component V_i can be interpreted as the effect on the variance of y when changing only x_i , V_{ij} is interpreted as the effect on the variance of y when changing x_i and x_j simultaneously, and so on.

The above components rescaled among the total variance of the function are known as global or Sobol sensitivity indices,

$$S_\ell = \frac{V_\ell}{Var(y)} \quad (30)$$

where ℓ represents the set of indices for a given combination of inputs. Hence, first-order indices S_i measure the contribution to the variance of y by a single input parameter, marginalizing the rest. On the other hand, the total effects indices S_{T_i} measure the contribution to the variance of y of an input parameter, as well as of its higher-order interactions with other parameters,

$$S_i = \frac{V_i}{Var(y)} \quad \text{and} \quad S_{T_i} = \frac{V_{T_i}}{Var(y)}. \quad (31)$$

In our case, we perform the described global sensitivity analysis using the SALib library in Python [56]. For the input parameters and their ranges, we consider those specified in Table 1. We base the input generation on the Sobol sequence, which is a low-discrepancy quasi-random sequence used to generate uniform samples of parameter space. Using a Saltelli sampling scheme [57], which extends the Sobol sequence to reduce the error rates in the resulting sensitivity index calculations, we generate a total of 28672 evaluations on our surrogate model, given by $N(2D+2)$, where $N=2048$ (number of samples) and $D=6$ (number of parameters). We adopted the recommendation that the value of N should ideally be a power of 2 [56]. Once the outputs are evaluated and obtained, via Monte Carlo integration we compute the total sensitivity indices for C_{rs} and R .

Furthermore, we want to observe how one of the model inputs (parameters) affects the output when all other parameters are averaged [58]. To accomplish this, using our ML surrogate model we compute the main effects of each model parameter, $z(X_i) = E(y|X_i) - E(y)$. Similar than in [30], to approximate this metric, we sample 100 trajectories from a latin hypercube design over the parameter space limited by the range specified in Table 1, varying the input X_i to compute the main effects across the parameter space.

2.8. Uncertainty quantification

A crucial task in our work is to propagate the uncertainties considered in the input parameters and quantify their impact on the output/lung response. This approach is usually called forward uncertainty quantification. Specifically, we sample from distributions defined for each input parameter, propagate these through our surrogate model, and then compute the empirical distribution of the response, y , thus having a problem of the form,

$$p(y) = p(f(\mathbf{X})) \quad (32)$$

where $p(y)$ is the probability of the response and $f(\mathbf{X})$ represents the mapping of our ML surrogate model from the input parameters to the lung response. Despite information on parameter variability in the literature, it was not possible to acquire information that characterizes the probability density of each parameter in our lung model, so in this work, we assume that each parameter follows a uniform distribution function of the form $x_i \sim U[a_i, b_i]$, where a_i and b_i are the lower and upper ranges specified in Table 1 for each parameter $x_i \in \mathbf{X}$, specifically. To choose the distribution sample size, we use as a criterion the coefficient of variation $CV = \sigma/\mu$, where σ is the standard deviation of

the means of a number m of uniform distributions each with sample size n , and μ is the average value of these means. Here, we choose $m = 1000$, and considering a criterion of $CV < 0.5\%$ as acceptable for the mean to be representative of the distributions, we vary the number of samples from $n = 100$ to 10000. With this considerations, the criterion is achieved for $n = 10000$ samples, with a $CV = 0.18\%$.

3. Results

3.1. Respiratory mechanics from dynamic finite element lung simulations

Fig. 2 shows a) airway pressure, b) flow rate, and c) lung volume signals of PCV ventilation mode, obtained from the high-fidelity and low-fidelity lung models that considered the baseline parameter values described in Table 1. Since our ventilation mode is pressure-controlled, the pressure signal is prescribed and therefore the same for both fidelity levels. Fig. 2d) shows the spatiotemporal evolution of the Jacobian field for high- and low-fidelity models in three key time instants of the ventilation cycle: time of peak flow ($t = 0.1s$), time of peak volume/end of inspiration ($t = 1s$) and time when half expiration has elapsed ($t = 2s$). This quantity gives an account of the local volumetric changes occurring in the lung. For the high-fidelity model, the Jacobian field displays a heterogeneous distribution, reaching values of volumetric change up to 1.3 at the end of inspiration and a state of zero volumetric deformation at expiration. For the low fidelity model, the Jacobian follows a similar range, although with a more homogeneous distribution. To quantify the error between the ventilation curves of the two fidelity models, we report the root-mean-square error (RMSE) considering the entire respiratory cycle. For the baseline case in high-fidelity simulations, the respiratory-system compliance was $C_{rs} = 93.62 \text{ ml/cm H}_2\text{O}$ and airways resistance was $R = 3.82 \text{ cm H}_2\text{O/L/s}$. For the low-fidelity model, we obtained $C_{rs} = 93.40 \text{ ml/cm H}_2\text{O}$ and $R = 4.09 \text{ cm H}_2\text{O/L/s}$. The high-fidelity simulation took ~ 2.7 hours while the low-fidelity simulation took ~ 2 min, which translates into a speed-up of $\sim 80\times$.

3.2. Performance assessment of machine learning models

Fig. 3 presents the performance of the three ML models in the testing set for respiratory-system compliance C_{rs} and resistance R . We show how the RMSE (mean and its standard deviation) evolves as more training samples are available for the multi-fidelity, single-fidelity, and neural network models. RMSE are reported in terms of equivalent high-fidelity cost, which is the cost of running a high-fidelity model. For the case of multi-fidelity, the curve is shifted to the right to account for the cost of 200 low-fidelity simulations.

From these results, it is observed that the multi-fidelity GP model, unlike the single-fidelity GP model and the neural network, achieves high prediction accuracy in both response variables, even with only 10 high-fidelity training samples. In this sense, it can be observed that the single-fidelity GP model and the neural network present errors and standard deviations of approximately one order of magnitude larger for C_{rs} . Despite this observation, it is worth noting that the single-fidelity GP decreases considerably its error in both responses as the training data size is increased, achieving for R a quite close performance to the multi-fidelity GP model. For both responses, the multi-fidelity GP model stabilizes around a training size of 14 samples (equivalent to a ratio 70/30% between training and validation), with an average RMSE of 1.2 and 0.015 for C_{rs} and R , respectively. Additionally, Figs. 4 and 5 show the correlation and Bland-Altman plots between the model predictions and the high-fidelity simulation values on each of the three models in comparison, for C_{rs} and R , respectively. The reported models were trained using 95% of the training data and were randomly selected from the cross-validation process. Consistent with the above result, the multi-fidelity GP model exhibits in overall the highest accuracy, with a value of $R^2 = 0.99$ for both responses, in conjunction with low standard deviations among the Bland-Altman differences. Also, for

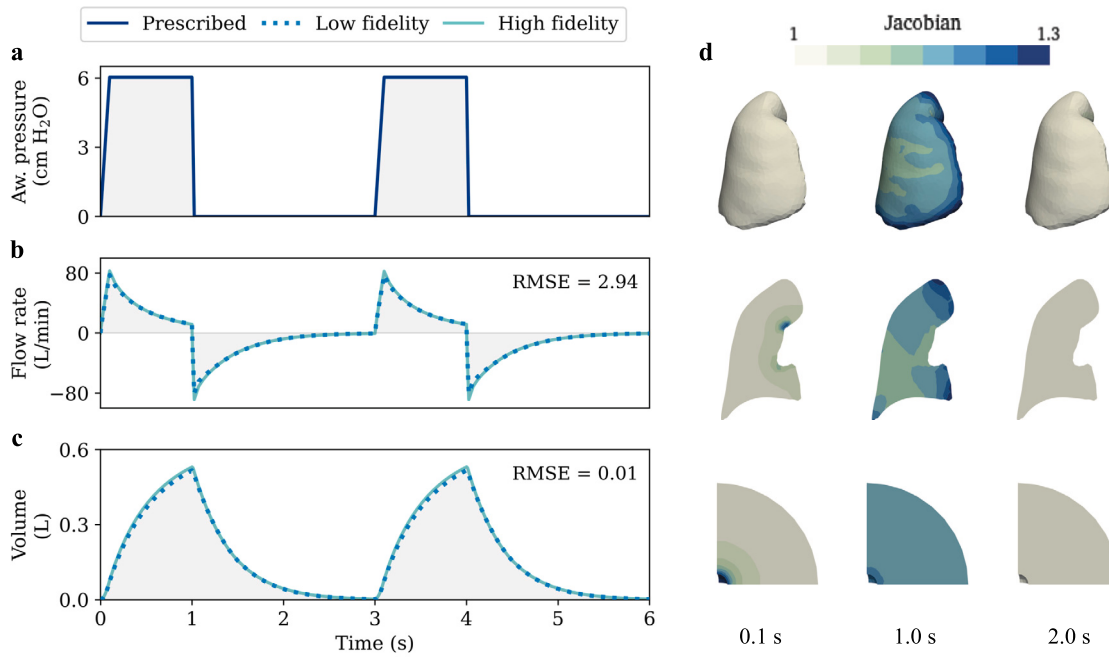


Fig. 2. Simulation of lungs under PCV ventilation model. Physiological signals that describe the time evolution of (a) airways pressure, (b) flow, and (c) volume (c) are shown for the high-fidelity (solid lines) and low-fidelity model (dashed lines). (d) Temporal evolution of the Jacobian field during a respiratory cycle for high-fidelity (1st and 2nd row) and low-fidelity (3rd row).

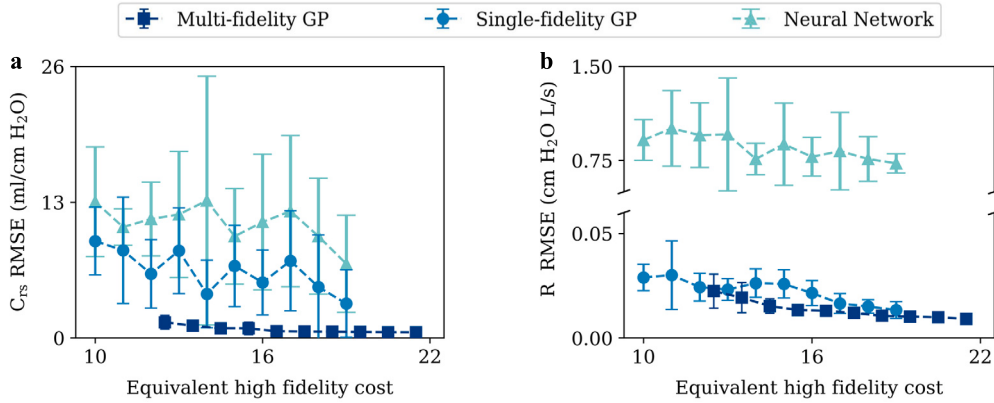


Fig. 3. Effect of the equivalent high-fidelity cost (training sample size) on the prediction performance of the multi-fidelity GP, single-fidelity GP, and neural network models. (a) Respiratory-system compliance, and (b) Resistance. Results shown are for the testing set predictions. Dashed lines and error bars denote the average and standard deviation of the RMSE, respectively.

C_{rs} predictions we observe that the neural network displays a quite acceptable performance, while the single-fidelity GP has the lowest one. An opposite trend is observed for R predictions, where in this case the neural network achieves even a negative R^2 (i.e. the trained model fits the data worse than a horizontal line). Regarding the uncertainty in the mean value predictions of the GPs, for C_{rs} and R the single-fidelity GP exhibits an average standard deviation of 9.27 and 0.32, while the multi-fidelity GP exhibits an average of 0.80 and 0.06. With these results in consideration, we chose the multi-fidelity GP as our definitive ML surrogate model to be applied in our subsequent sensitivity, main effects, and uncertainty quantification analysis. In terms of time, our multi-fidelity model takes approximately 0.01 s to perform a prediction, which implies a speed-up of $\sim 970,000\times$ with respect to the time taken to run one high-fidelity simulation.

3.3. Sensitivity analysis in respiratory response

Fig. 6 shows the Sobol total-order sensitivity indices along with their 95% confidence interval for respiratory-system compliance C_{rs} and re-

sistance R . Regarding the compliance, the constitutive model parameter c has the greatest influence on it, with an index of ~ 0.47 , followed closely by the chest wall stiffness K_s with an index of ~ 0.40 , and with β and k having a smaller influence. On the other hand, permeability k is the only parameter that has a considerable influence on the resistance, with an index of ~ 1 . Interestingly, parameters c_1 and c_3 show no influence in predicting compliance or resistance values.

3.4. Main effects analysis

The main effects of each input parameter on respiratory-system compliance C_{rs} and airways resistance R are shown in Figs. 7 and 8, respectively, where 100 trajectories are included for each parameter under analysis in order to compute the response effect associated with changes in the respective parameter. Interestingly, C_{rs} displays a decreasing relation with tissue constitutive parameters c , β , and the chest-wall stiffness K_s . The latter also shows a marked non-linear dependence. From the amplitude of trajectories ensemble in 7, we observe that c is the most influential parameter on C_{rs} , followed closely by K_s .

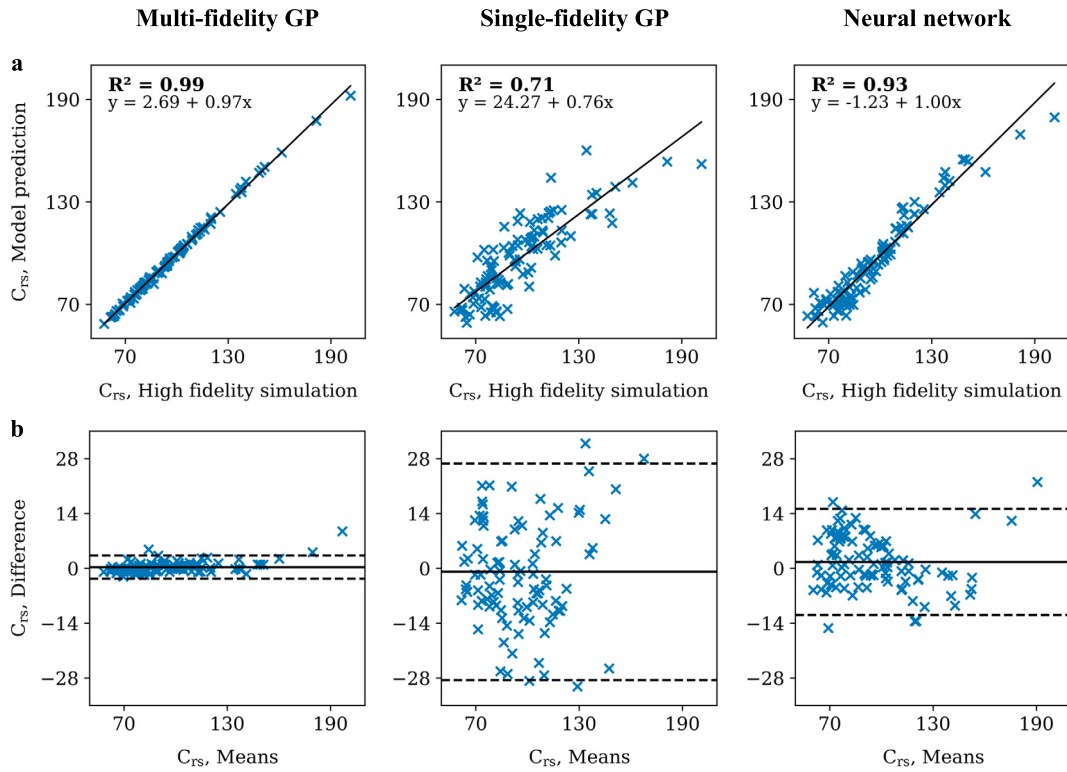


Fig. 4. Performance comparison of multi-fidelity GP, single-fidelity GP, and neural network models on the respiratory-system compliance. All units are in ml/cm H₂O. Regarding the high-fidelity data for training, each model was trained with a training size of 95% (19 observations). The predictions on the testing set are analyzed using (a) correlation plots, and (b) Bland-Altman plots. In Bland-Altman plots, solid lines represent the mean difference between the high-fidelity simulations and model predictions, while dashed lines represent their corresponding ± 1.96 standard deviations.

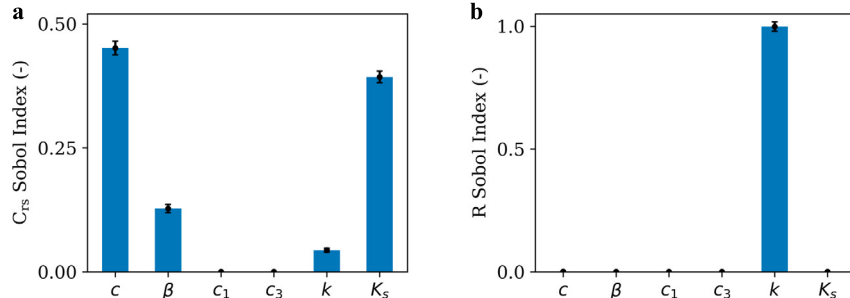


Fig. 5. Performance comparison of multi-fidelity GP, single-fidelity GP and neural network models on the airways resistance. All units are in cm H₂O/L/s. Regarding the high-fidelity data for training, each model was trained with a training size of 95% (19 observations). The predictions on the testing set are analyzed using (a) correlation plots, and (b) Bland-Altman plots. In Bland-Altman plots, solid lines represent the mean difference between the high-fidelity simulations and model predictions, while dashed lines represent their corresponding ± 1.96 standard deviations.

Tissue permeability k presents a slightly increasing relationship with compliance. Parameters c_1 and c_3 display a very low influence on C_{rs} . In the case of airway resistance, we observe that the only parameter that shows a considerable influence is the permeability k , with a non-linear decreasing relationship, see Fig. 8. The fact that this is the only influential parameter is also inferred from the highly concentrated lines in the plot of k .

3.5. Variability of respiratory-system compliance and resistance

Fig. 9 shows an example of how uncertainty in the constitutive parameter c propagates through the ML lung model, affecting the compliance and resistance of the system. We modeled c as a uniform distribution with bounds of $\pm 25\%$ of the baseline value. On the left side of Fig. 9, we show the empirical uniform distribution that characterizes c , where the vertical line corresponds to the baseline value reported in

Table 1. On the right, we show the distributions of possible values of the response along with their probability density functions, where the vertical lines correspond to C_{rs} and R obtained for the baseline parameters, which we identify with the reference response of the lung. For the case of C_{rs} , we observe linearly decreasing density function. An opposite trend is observed for R , where the density increases with higher values of resistance.

Fig. 10 shows the uncertainty propagation analysis for each of the six model parameters considered in our study. We also report the case of uncertainty in all parameters simultaneously. To understand how the degree of variability in input parameters affects the lung response, we considered three levels for the input uniform distribution bounds: $\Delta = \pm 10\%, \pm 25\%, \pm 50\%$. In general, the density functions for C_{rs} and R display a higher spread as Δ increases. The higher variability in C_{rs} is mainly due to the uncertainty added in parameters c and K_s . In contrast, uncertainty in c_1 and c_2 results in almost no variability in C_{rs} . For

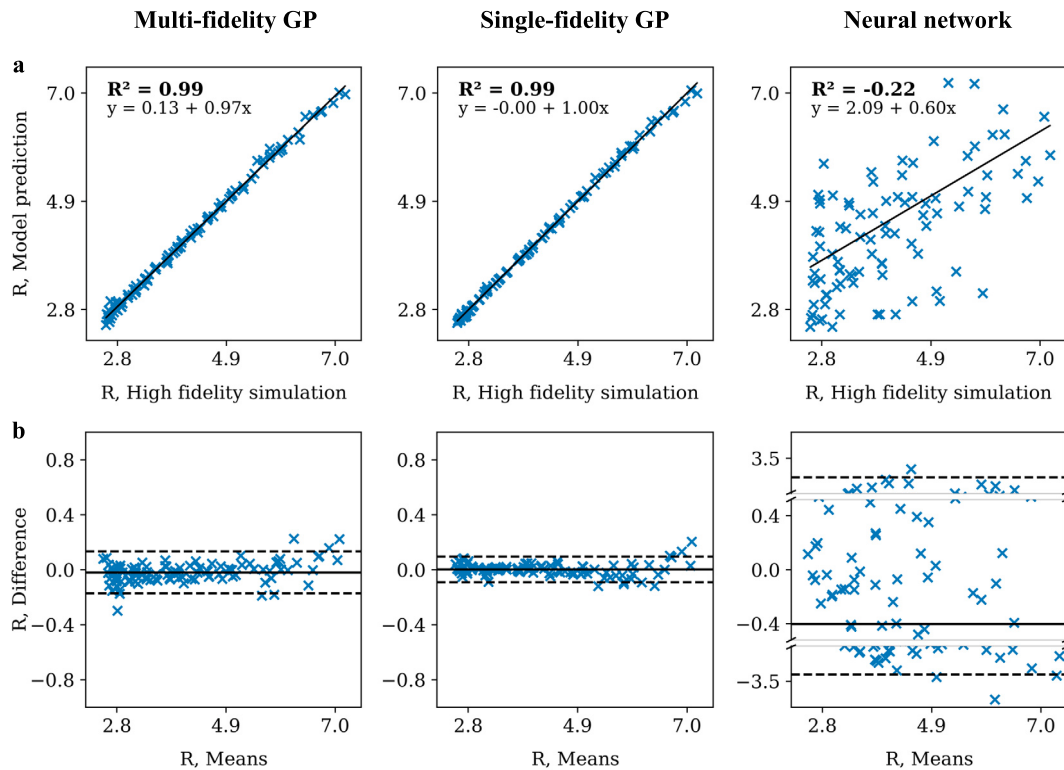


Fig. 6. Sobol total sensitivity indices with respect to lung model parameters [c , β , c_1 , c_3 , k , K_s], for (a) respiratory-system compliance, and (b) airways resistance. Each bar indicates the total-order index, while error bars indicate the 95% confidence intervals.

R , uncertainty in the permeability k shows a considerable influence on the system response, while uncertainty in all other input parameters results in negligible variability of the resistance. We also observe that, in general, the distributions of both C_{rs} and R are slightly right-skewed. When uncertainty is considered in all parameters simultaneously, the response on C_{rs} shows a Gaussian shape distribution. Table 2 summarizes the values for the mean, 2.5% ($P_{2.5}$) and 97.5% ($P_{97.5}$) percentile of the obtained distributions. From these results, we note that the largest variability in compliance C_{rs} and resistance R occur when uncertainty is added in all parameters simultaneously.

4. Discussion

In this work, we have constructed models of lung mechanics using ML techniques, which are informed by nonlinear FE poromechanical simulations. Fig. 2 shows that both high- and low-fidelity FE simulations predict the ventilatory curves typically observed in real patients connected to MV [43]. The respiratory-mechanics parameters predicted by these simulations are in good agreement with the clinical literature: respiratory-system compliance C_{rs} is within acceptable values (50 - 100 $\text{ml}/\text{cm H}_2\text{O}$) for normal lungs [43,59], and airways resistance R falls within the range reported for normal subjects under ventilatory support (< 15 - 20 $\text{cm H}_2\text{O/L/s}$) [60]. It is interesting to note that the low-fidelity FE model delivers a global lung response that is very close to that predicted by high-fidelity simulations at a fraction of the computational time that is almost two orders of magnitude smaller.

A crucial objective of this work was to build ML lung-mechanics models that were both predictive and efficient. Figs. 3(a) and 3(b) show that the multi-fidelity GP model consistently delivers better accuracy than the single-fidelity GP and neural network models in estimating respiratory-system compliance and resistance, respectively. In particular, it is interesting to note that this advantage of the multi-fidelity GP model is obtained even for the case where only 10 high-fidelity simulations were used for training. Figs. 4 and 5 further show that not only the average error associated with the multi-fidelity GP model is low, but it

Table 2

Statistics for the probability density function of respiratory-system compliance, and resistance with respect to each level of parameter uncertainty.

Parameter	$\Delta =$	C_{rs} ($\text{ml}/\text{cm H}_2\text{O}$)			R ($\text{cm H}_2\text{O L/s}$)		
		$\pm 10\%$	$\pm 25\%$	$\pm 50\%$	$\pm 10\%$	$\pm 25\%$	$\pm 50\%$
c	Mean	94.04	94.41	95.84	3.82	3.81	3.80
	$P_{2.5}$	88.96	82.28	73.04	3.80	3.76	3.66
	$P_{97.5}$	99.34	108.23	124.67	3.83	3.85	3.87
β	Mean	93.98	94.11	94.61	3.82	3.82	3.84
	$P_{2.5}$	91.22	87.41	81.47	3.82	3.82	3.82
	$P_{97.5}$	96.82	101.52	110.5	3.82	3.84	3.92
c_1	Mean	93.94	93.89	93.75	3.82	3.82	3.83
	$P_{2.5}$	93.89	93.74	93.43	3.82	3.82	3.82
	$P_{97.5}$	93.96	93.96	93.95	3.83	3.84	3.85
c_3	Mean	93.94	93.94	93.91	3.82	3.82	3.82
	$P_{2.5}$	93.88	93.77	93.59	3.81	3.80	3.80
	$P_{97.5}$	94.01	94.08	94.12	3.82	3.83	3.85
k	Mean	93.90	93.70	92.89	3.83	3.89	4.13
	$P_{2.5}$	92.53	89.85	83.10	3.50	3.11	2.51
	$P_{97.5}$	95.14	96.63	98.42	4.20	4.95	6.94
K_s	Mean	94.04	94.54	96.67	3.82	3.82	3.83
	$P_{2.5}$	89.87	84.52	77.06	3.81	3.81	3.81
	$P_{97.5}$	98.61	106.84	125.38	3.83	3.85	3.89
<i>All</i>	Mean	94.10	95.00	98.02	3.83	3.90	4.18
	$P_{2.5}$	85.78	75.47	61.23	3.50	3.11	2.60
	$P_{97.5}$	103.42	121.07	160.91	4.20	4.96	6.96

also delivers a very low dispersion in its estimates when compared to the single-fidelity GP and neural network models. Incorporating GPs into our study offered a pivotal advantage: the ability to furnish predictions along with their corresponding variances, allowing for a robust quantification of uncertainty surrounding the predictive mean value and assessing the reliability of model predictions. Notably, our multi-

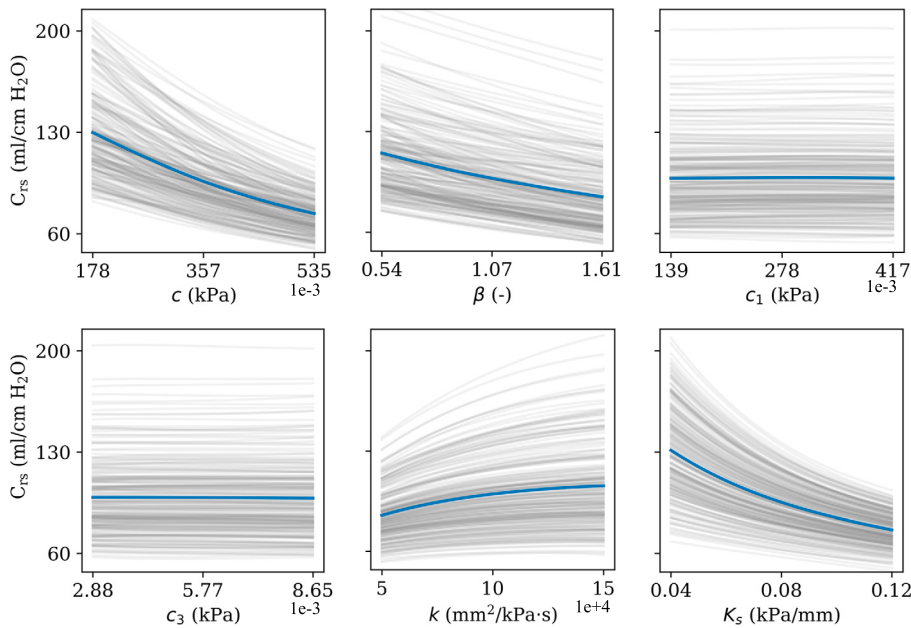


Fig. 7. Main effects analysis of each model parameter on the respiratory-system compliance C_{rs} . Parameters c , β and K_s show an inverse relationship with compliance. Furthermore, c and K_s have the greatest influence on the response. On the other hand, k shows a slightly direct relation with compliance. Parameters c_1 and c_3 do not influence the response of compliance. In each subfigure, gray lines represent the 100 trajectories used for the simulation, while the blue line represent the average main effect of the sampled trajectories.

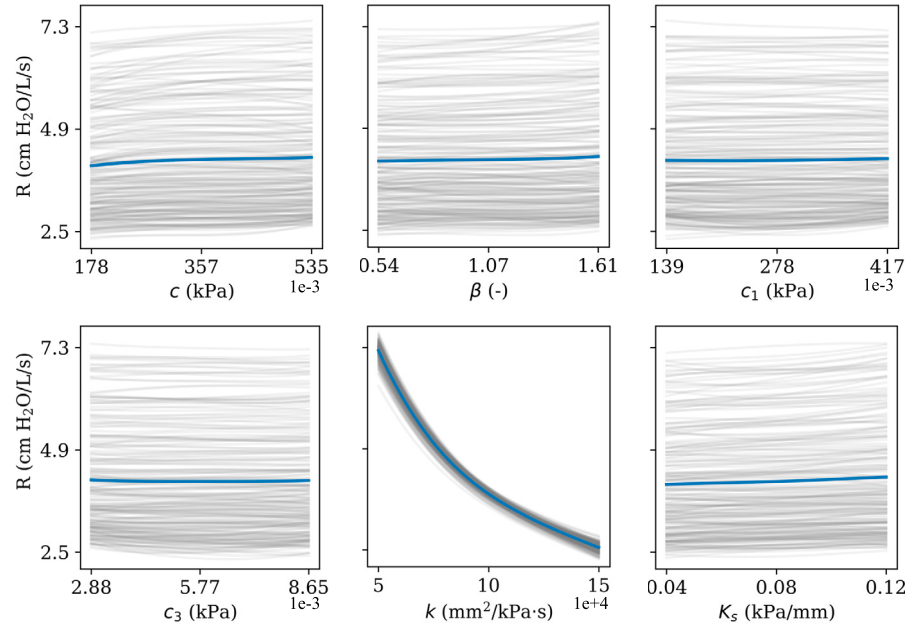


Fig. 8. Main effects analysis of each model parameter on the airways resistance R . The permeability parameter k is the only one with influence on the response. It can be observed that this parameter shows a non-linear inverse relationship with resistance. In each figure, gray lines represent the 100 trajectories used for the simulation, while the blue line represent the average main effect of the sampled trajectories.

fidelity GP model not only enhanced predictive means accuracy but also demonstrated a substantial reduction in prediction uncertainty, as consistently observed in our results. This excellent performance of the multi-fidelity model can be explained by the high level of prediction achieved by the low-fidelity model, as seen in Fig. 2. These findings highlight the convenience of developing low-fidelity models that deliver attractive accuracy-efficient trade-offs, which can be implemented in multi-fidelity methods, similar to what has been reported for other biophysical systems in the literature [30,31]. Regarding the GP regression, the discrepancy in the accuracy of compliance and resistance predictions could be partly due to the fact that these variables differ

by at least an order of magnitude, so the higher variance of the former could influence the optimization process when training the model, yielding in poor prediction performance. Therefore, a possible solution to this would be to also scale the output variables. Additionally, we must consider that a better performance is expected when training the single-fidelity GP model with a larger dataset, as shown in Fig. 3(a). However, it is crucial to emphasize that while GPs offer greater interpretability than neural networks due to their structure, they are mostly suitable for modeling small datasets since their effectiveness diminishes when dealing with high-dimensionality, as in their naive formulation the computational cost scale in order $O(n^3)$ for a data size n [61]. Given

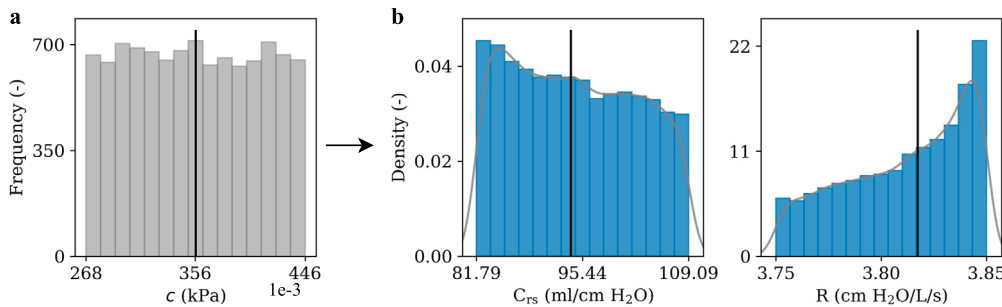


Fig. 9. Uncertainty propagation of constitutive model parameter c and its effect on the response variability. This example considers an uncertainty of $\Delta = \pm 25\%$ around the baseline value, where (a) corresponds to the uniform probability distribution of parameter c , which is applied to our surrogate model, obtaining in (b) empirical distributions for respiratory-system-compliance and resistance response. Vertical lines represent the baseline value in (a) and the corresponding compliance and resistance values in (b). Solid gray curves represent the corresponding probability density functions.

this constraint, neural networks may prove more suitable for handling a larger dataset, while also delivering a better performance. Regarding computational efficiency, we highlight that our ML model delivers a speed-up in the computation of compliance and resistance of approximately 970,000 \times with respect to the high-fidelity simulation. This massive boost is tremendously interesting from a clinical applications perspective, where computational time is a critical factor in technology adoption. However, we must keep in mind that our low-fidelity FE model, despite the marked homogeneity in the spatiotemporal response due to the use of an idealized geometry (Fig. 2(d)), can be considered sufficient in terms of computational efficiency for its application in the prediction of global variables (compliance and resistance), although not as advantageous for UQ analysis, which usually requires a large number of simulations. In particular, our results confirm the ability of ML techniques to accelerate computational simulations in biophysics and biomechanics, whose application has been reported in the literature for other organs of the human body [62,17,18].

A relevant application of our ML model of lung function is the sensitivity analysis of how constitutive parameters affect lung response. From this perspective, the constitutive model parameters of lung tissue c and β , in conjunction with the mechanical chest wall parameter K_s were found to be the most influential on the compliance of the respiratory system C_{rs} , as shown in Fig. 6(a). It is also interesting to note that the parameters c_1 and c_3 have no relevance in the overall elastic response of the lung. The same conclusions are reached from the main effects analysis, see Fig. 7, which unveils the insensitivity of C_{rs} to changes in c_1 and c_3 . Additionally, the main effects analysis shows that the relationship between the parameters c , β , K_s , and C_{rs} is nonlinear. Further, we note that C_{rs} decreases with increasing values of these parameters. The relevance of these three constitutive model parameters in the determination of lung function highlights the need of experiments that enable a precise characterization of these parameters for healthy and pathological conditions of the lung. At the same time, our results question the relevance of constitutive parameters c_1 and c_3 in the tissue response and strain energy function proposed in [37], which invites us to revisit the current constitutive models with a global function perspective. In addition, an important conclusion of our work is that the stiffness imposed by the chest wall, represented in our simulations by the spring stiffness coefficient K_s , has a level of influence comparable to that of the lung tissue elasticity modulated by the parameter c . The latter is mutually complemented by the fact that, in classical respiratory physiology, where single compartment models are used, the respiratory-system compliance C_{rs} considers the contribution of both the lung C_l and the chest wall C_{cw} [43] compliance. This highlights the importance of future works of being able to mechanistically characterize the interaction of the lung with neighboring organs and structures such as the diaphragm and mediastinum.

Another significant result of our sensitivity analysis is the strong dependence of the airways resistance R on the permeability parameter

k , as well as the low dependence on the remaining constitutive parameters, see Fig. 6(b). This conclusion also emerges from the main effect analysis, where only the parameter k has a nonlinear and decreasing influence on R , while changes in the other parameters do not affect it (Fig. 8). This result can be explained by the continuous approach adopted for the alveolar airflow, which is strongly driven by pressure gradients and modulated mainly by the permeability tensor κ in Darcy's law [11]. In particular, these results show that tissue deformability in the explored range does not seem to have an influence on air propagation through the lung tissue, i.e., airflow is weakly coupled to lung tissue deformation in our model. It is interesting to mention that this weak coupling has been observed in other multiphysics deformable models with a mathematical structure similar to the one proposed by the considered poromechanical model in our study, such as cardiac electromechanical models, where the deformation modulates the spatial propagation of electrical waves governed by Laplacian operators in the spatial configuration [38,63].

Uncertainty in some of the input parameters can have a substantial impact on the overall respiratory-system mechanics, see Fig. 9. Table 2 shows that when we introduce an uncertainty level of $\pm 50\%$ into c , the most sensitive parameter, the resulting compliance C_{rs} can vary between $P_{2.5} = 73 \text{ ml/cm H}_2\text{O}$ and $P_{97.5} = 125 \text{ cm H}_2\text{O L/s}$ with 95% probability. This implies that, in relative terms, C_{rs} can vary around its reference value between -22% and +34%. A similar analysis on the chest wall stiffness parameter K_s leads to a range between -18% and +34% of the reference value. Thus, this level of variability in these two parameters is enough to reach compliance values that can be considered pathological, as discussed before [43]. In the case of airway respiratory-system resistance, a $\pm 50\%$ uncertainty in the permeability parameter k introduces a response variability of -34% and +84% around the baseline resistance value. Uncertainty in other input parameters does not affect resistance, see Fig. 10, a result that is in line with our conclusions from the parameter sensitivity study. Our results show that sensitivity analysis, main effects analysis, and uncertainty quantification each offer unique and complementary advantages. Sensitivity analysis provides valuable insights into the influence of individual parameters on model outputs, allowing easy identification of key drivers of model behavior in relation to lung function. Main effects analysis further refines this understanding by exhibiting how an individual parameter affects the outcome, independent of interactions with other parameters. Meanwhile, uncertainty quantification offers a broader perspective by quantifying this impact and considering the combined effect of uncertainties in all input parameters on lung response. Together, these methods can form a powerful toolkit for understanding and managing the inherent uncertainties in the study of complex biomechanical models, as shown here.

Our work represents a proof of concept of the potential and applications of ML lung models informed by poromechanical simulations, which offer many opportunities for improvement and future develop-

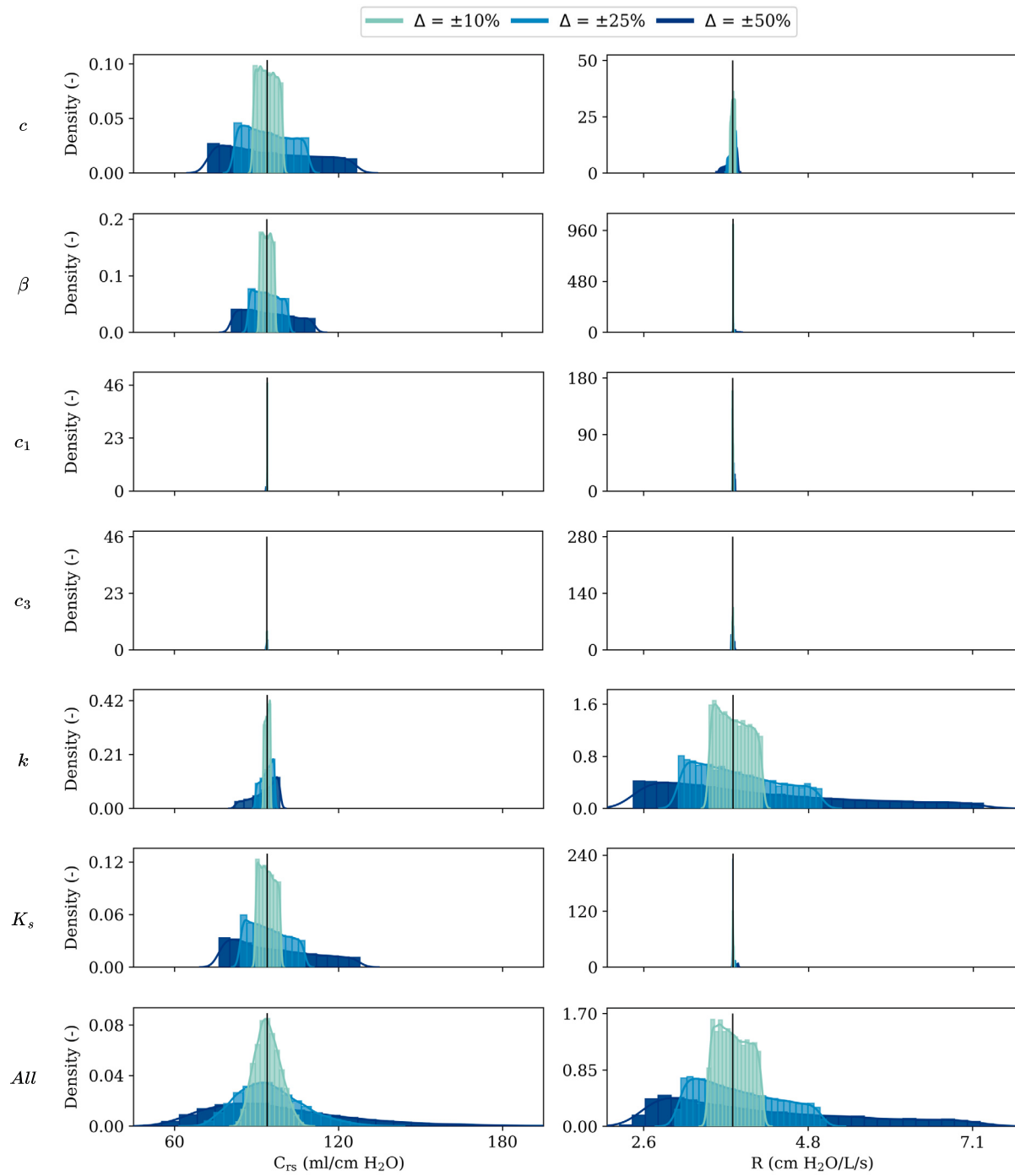


Fig. 10. Uncertainty propagation analysis for respiratory-system compliance and airways resistance. Three levels of variability in the input probability distribution are considered: $\Delta = \pm 10\%, \pm 25\%, \pm 50\%$. Each row corresponds to one of the six parameters [c , β , c_1 , c_3 , k , K_s]. The last row shows the variability when uncertainty is present in all parameters simultaneously (All). Vertical lines correspond to values obtained for the baseline parameters.

ments. First, while the efficiency and accuracy of the multi-fidelity GP model are very promising, we note that it is constructed using fixed lung domains with homogeneous properties. While some of these assumptions may hold in normal lungs [64], they do not adequately capture the morphological variability nor mechanical heterogeneity observed in the lung during pathological cases [65,66]. To transition to a fully personalized framework, future contributions should consider lung anatomy and structural heterogeneity as input parameters and deformation and stress fields as output quantities. This will necessitate the consideration of high-dimensional input and output spaces, which have been approached using multi-output Gaussian Processes [67–70] and

physics-informed neural networks, which are more suitable to handle larger high-dimensional input datasets [71]. Second, in carrying out UQ analysis, we have assumed that input parameters have a uniform probability distribution. This decision was motivated by the lack of statistical characterization of these parameters and represents a conservative approach [24]. However, improving the accuracy and applicability of our approach necessitates a data-driven experimental characterization of the input parameter uncertainty, as done for cardiac electrophysiological systems [72]. Lastly, using a phenomenological constitutive model for our lung simulations has enabled the feasibility of this study in terms of computational costs. However, phenomenological models lack phys-

ical interpretation and predictive power compared to micromechanical lung tissue models [73,74]. Future extensions of this work could consider a multiscale poromechanical lung framework to inform and validate ML lung models [75]. As presented in this work, this represents an opportunity to both accelerate multiscale simulations and understand the impact of microstructural parameters on the overall response of lungs under MV.

Declaration of competing interest

The authors declare that they have no known competing financial interests or personal relationships that could have appeared to influence the work reported in this paper.

Acknowledgements

This work received financial support from the Chilean National Agency for Research and Development (ANID) FONDECYT Regular #1220465 and from graduate fellowship ANID BECAS/DOCTORADO NACIONAL #21220063.

References

- [1] Deepak K. Agrawal, Bradford J. Smith, Peter D. Sottile, David J. Albers, A damaged-informed lung ventilator model for ventilator waveforms, *Front. Physiol.* 12 (October 2021).
- [2] Covid-19 map, <https://coronavirus.jhu.edu/map.html>, 2023.
- [3] Christopher M. Petrilli, Simon A. Jones, Jie Yang, Harish Rajagopalan, Luke O'Donnell, Yelena Chernyak, Katie A. Tobin, Robert J. Cerfolio, Fritz Francois, Leora I. Horwitz, Factors associated with hospital admission and critical illness among 5279 people with coronavirus disease 2019 in New York City: prospective cohort study, *BMJ* 369 (2020) m1966.
- [4] Giacomo Grasselli, Alberto Zangrillo, Alberto Zanella, Massimo Antonelli, Luca Cabrini, Antonio Castelli, Danilo Cereda, Antonio Coluccello, Giuseppe Foti, Roberto Fumagalli, et al., Baseline characteristics and outcomes of 1591 patients infected with Sars-cov-2 admitted to icus of the lombardy region, Italy, *JAMA* 323 (16) (2020) 1574–1581.
- [5] Huiqing Ge, Qing Pan, Yong Zhou, Peifeng Xu, Lingwei Zhang, Junli Zhang, Jun Yi, Changming Yang, Yuhua Zhou, Limin Liu, et al., Lung mechanics of mechanically ventilated patients with Covid-19: analytics with high-granularity ventilator waveform data, *Front. Med.* 7 (2020) 541.
- [6] Gianluigi Li Bassi, Jacky Y. Suen, Heidi J. Dalton, Nicole White, Sally Shrapnel, Jonathon P. Fanning, Benoit Liquet, Samuel Hinton, Aapeli Vuorinen, Gareth Booth, et al., An appraisal of respiratory system compliance in mechanically ventilated Covid-19 patients, *Crit. Care* 25 (1) (2021) 199.
- [7] Giacomo Grasselli, Emanuele Cattaneo, Gaetano Florio, Mariachiara Ippolito, Alberto Zanella, Andrea Cortegiani, Jianbo Huang, Antonio Pesenti, Sharon Einav, Mechanical ventilation parameters in critically ill Covid-19 patients: a scoping review, *Crit. Care* 25 (2021) 1–11.
- [8] Lorenz Berger, Rafel Bordas, Kelly Burrowes, Vicente Grau, Simon Tavener, David Kay, A poroelastic model coupled to a fluid network with applications in lung modelling, *Int. J. Numer. Methods Biomed. Eng.* 32 (1) (2016).
- [9] Martin Genet, Cécile Patte, Catalin Fetita, P-Y. Brillet, D. Chapelle, Personalized pulmonary poromechanics, *Comput. Methods Biomed. Eng.* 23 (sup1) (2020) S119–S120.
- [10] Cécile Patte, Martin Genet, Dominique Chapelle, A quasi-static poromechanical model of the lungs, *Biochem. Model. Mechanobiol.* 21 (2) (2022) 527–551.
- [11] Nibaldo Avilés-Rojas, Daniel E. Hurtado, Whole-lung finite-element models for mechanical ventilation and respiratory research applications, *Front. Physiol.* 13 (October 2022).
- [12] Amirsossein Arzani, Jian-Xun Wang, Michael S. Sacks, Shawn C. Shadden, Machine learning for cardiovascular biomechanics modeling: challenges and beyond, *Ann. Biomed. Eng.* 50 (6) (2022) 615–627.
- [13] Mathias Peirlinck, F. Sahli Costabal, K.L. Sack, J.S. Choy, G.S. Kassab, J.M. Guccione, M. De Beule, Patrick Segers, E. Kuhl, Using machine learning to characterize heart failure across the scales, *Biomech. Model. Mechanobiol.* 18 (2019) 1987–2001.
- [14] Francisco Sahli Costabal, Yibo Yang, Paris Perdikaris, Daniel E. Hurtado, Ellen Kuhl, Physics-informed neural networks for cardiac activation mapping, *Front. Phys.* 8 (2020) 42.
- [15] Liang Liang, Minliang Liu, Caitlin Martin, Wei Sun, A deep learning approach to estimate stress distribution: a fast and accurate surrogate of finite-element analysis, *J. R. Soc. Interface* 15 (138) (2018) 20170844.
- [16] Gaoyang Li, Haoran Wang, Mingzi Zhang, Simon Tupin, Aike Qiao, Youjun Liu, Makoto Ohta, Hitomi Anzai, Prediction of 3d cardiovascular hemodynamics before and after coronary artery bypass surgery via deep learning, *Commun. Biol.* 4 (1) (2021) 99.
- [17] Taeksang Lee, Arun K. Gosain, Ilias Bilionis, Adrian Buganza Tepole, Predicting the effect of aging and defect size on the stress profiles of skin from advancement, rotation and transposition flap surgeries, *J. Mech. Phys. Solids* 125 (2019) 572–590.
- [18] Oscar J. Pellicer-Valero, María José Rupérez, Sandra Martínez-Sanchis, José D. Martín-Guerrero, Real-time biomechanical modeling of the liver using machine learning models trained on finite element method simulations, *Expert Syst. Appl.* 143 (2020) 113083.
- [19] Tao Peng, Yihuai Wang, Thomas Canhao Xu, Lianmin Shi, Jianwu Jiang, Shilang Zhu, Detection of lung contour with closed principal curve and machine learning, *J. Digit. Imag.* 31 (2018) 520–533.
- [20] Qinhua Hu, Luis Fabricio de F Souza, Gabriel Bandeira Holanda, Shara S.A. Alves, Francisco Hercules dos S Silva, Tao Han, Pedro P. Reboucas Filho, An effective approach for ct lung segmentation using mask region-based convolutional neural networks, *Artif. Intell. Med.* 103 (2020) 101792.
- [21] Elsa Angelini, Simon Dahan, Anand Shah, Unravelling machine learning: insights in respiratory medicine, *Eur. Respir. J.* 54 (6) (2019).
- [22] Alan Kaplan, Hui Cao, J. Marl FitzGerald, Nick Iannotti, Eric Yang, Janwillem W.H. Kocks, Konstantinos Kostikas, David Price, Helen K. Reddel, Ioanna Tsiliogianni, et al., Artificial intelligence/machine learning in respiratory medicine and potential role in asthma and copd diagnosis, *J. Allergy Clin. Immunol.* 9 (6) (2021) 2255–2261.
- [23] Sanjay Sarma Oruganti Venkata, Amie Koenig, Ramana M. Pidaparti, Mechanical ventilator parameter estimation for lung health through machine learning, *Bioengineering* 8 (5) (2021) 60.
- [24] Daniel E. Hurtado, Sebastián Castro, Pedro Madrid, Uncertainty quantification of 2 models of cardiac electromechanics, *Int. J. Numer. Methods Biomed. Eng.* 33 (12) (2017) e2894.
- [25] J.O. Campos, J. Sundnes, R.W. Dos Santos, B.M. Rocha, Uncertainty quantification and sensitivity analysis of left ventricular function during the full cardiac cycle, *Philos. Trans. R. Soc. A* 378 (2017) 20190381.
- [26] Elias Karabelas, Stefano Longobardi, Jana Fuchsberger, Orod Razeghi, Cristobal Rodero, Marina Strocchi, Ronak Rajani, Gundolf Haase, Gernot Plank, Steven Niederer, Global sensitivity analysis of four chamber heart hemodynamics using surrogate models, *IEEE Trans. Biomed. Eng.* 69 (10) (2022) 3216–3223.
- [27] Marina Strocchi, Stefano Longobardi, Christoph M. Augustin, Matthias A.F. Gsell, Argyrios Petras, Christopher A. Rinaldi, Edward J. Vigmond, Gernot Plank, Chris J. Oates, Richard D. Wilkinson, et al., Cell to whole organ global sensitivity analysis on a four-chamber heart electromechanics model using Gaussian processes emulators, *PLoS Comput. Biol.* 19 (6) (2023) e1011257.
- [28] Justin Garrish, Christine Chan, Douglas Nychka, Cecilia Diniz Behn, A Gaussian process model for insulin secretion reconstruction with uncertainty quantification: applications in cystic fibrosis, *SIAM J. Appl. Math.* (2023) S65–S81.
- [29] Dongwei Ye, Pavel Zun, Valeria Krzhizhanovskaya, Alfons G. Hoekstra, Uncertainty quantification of a three-dimensional in-stent restenosis model with surrogate modelling, *J. R. Soc. Interface* 19 (187) (2022) 20210184.
- [30] Francisco Sahli Costabal, Kristen Matsuno, Jiang Yao, Paris Perdikaris, Ellen Kuhl, Machine learning in drug development: characterizing the effect of 30 drugs on the QT interval using Gaussian process regression, sensitivity analysis, and uncertainty quantification, *Comput. Methods Appl. Mech. Eng.* 348 (May 2019) 313–333.
- [31] Taeksang Lee, Ilias Bilionis, Adrian Buganza Tepole, Propagation of uncertainty in the mechanical and biological response of growing tissues using multi-fidelity Gaussian process regression, *Comput. Methods Appl. Mech. Eng.* 359 (February 2020) 112724.
- [32] Tianhong Han, Kaleem S. Ahmed, Arun K. Gosain, Adrian Buganza Tepole, Taeksang Lee, Multi-fidelity Gaussian process surrogate modeling of pediatric tissue expansion, *J. Biomech. Eng.* 144 (12) (2022) 121005.
- [33] Lia Gander, Simone Pezzuto, Ali Gharaviri, Rolf Krause, Paris Perdikaris, Francisco Sahli Costabal, Fast characterization of inducible regions of atrial fibrillation models with multi-fidelity Gaussian process classification, *Front. Physiol.* (2022) 260.
- [34] Mohammad Motamed, A multi-fidelity neural network surrogate sampling method for uncertainty quantification, *Int. J. Uncertain. Quantificat.* 10 (4) (2020).
- [35] Xuhui Meng, George Em Karniadakis, A composite neural network that learns from multi-fidelity data: application to function approximation and inverse pde problems, *J. Comput. Phys.* 401 (2020) 109020.
- [36] Mengwu Guo, Andrea Manzoni, Maurice Amendt, Paolo Conti, Jan S. Hesthaven, Multi-fidelity regression using artificial neural networks: efficient approximation of parameter-dependent output quantities, *Comput. Methods Appl. Mech. Eng.* 389 (2022) 114378.
- [37] Anna M. Birzle, Christian Martin, Stefan Uhlig, Wolfgang A. Wall, A coupled approach for identification of nonlinear and compressible material models for soft tissue based on different experimental setups – exemplified and detailed for lung parenchyma, *J. Mech. Behav. Biomed. Mater.* 94 (June 2019) 126–143.
- [38] Daniel E. Hurtado, Nicolás Villarroel, Carlos Andrade, Jaime Retamal, Guillermo Buggedo, Alejandro Bruhn, Spatial patterns and frequency distributions of regional deformation in the healthy human lung, *Biomech. Model. Mechanobiol.* 16 (4) (March 2017) 1413–1423.
- [39] Daniel E. Hurtado, Nicolas Villarroel, Jaime Retamal, Guillermo Buggedo, Alejandro Bruhn, Improving the accuracy of registration-based biomechanical analysis: a finite element approach to lung regional strain quantification, *IEEE Trans. Med. Imaging* 35 (2) (February 2016) 580–588.

- [40] Martin Alnæs, Jan Blechta, Johan Hake, August Johansson, Benjamin Kehlet, Anders Logg, Chris Richardson, Johannes Ring, Marie E. Rognes, Garth N. Wells, The fenics project version 1.5, *Arch. Numer. Softw.* 3 (2015).
- [41] Christophe Geuzaine, Jean-François Remacle, Gmsh: a 3-d finite element mesh generator with built-in pre- and post-processing facilities, *Int. J. Numer. Methods Eng.* 79 (11) (May 2009) 1309–1331.
- [42] Lony Ashworth, Yasuhiro Norisue, Megan Koster, Jeff Anderson, Junko Takada, Hatsuyo Ebisu, Clinical management of pressure control ventilation: an algorithmic method of patient ventilatory management to address “forgotten but important variables”, *J. Crit. Care* 43 (February 2018) 169–182.
- [43] Dean R. Hess, Respiratory mechanics in mechanically ventilated patients, *Respir. Care* 59 (11) (October 2014) 1773–1794.
- [44] Giacomo Bellani, Mechanical Ventilation from Pathophysiology to Clinical Evidence, Springer, 2022.
- [45] Zachary Edwards, Pavan Annamaraju, Physiology, Lung Compliance, *StatPearls*, 2020.
- [46] Carl Edward Rasmussen, Christopher K.I. Williams, et al., Gaussian Processes for Machine Learning, vol. 1, Springer, 2006.
- [47] Andreas C. Damianou, Michalis K. Titsias, Neil D. Lawrence, Variational inference for latent variables and uncertain inputs in Gaussian processes, *J. Mach. Learn. Res.* 17 (42) (2016) 1–62.
- [48] Marc C. Kennedy, Anthony O'Hagan, Predicting the output from a complex computer code when fast approximations are available, *Biometrika* 87 (1) (2000) 1–13.
- [49] Abien Fred Agarap, Deep learning using rectified linear units (relu), *CoRR*, arXiv: 1803.08375 [abs], 2018.
- [50] Diederik P. Kingma, Jimmy Ba, Adam: a method for stochastic optimization, *arXiv preprint, arXiv:1412.6980*, 2014.
- [51] F. Pedregosa, G. Varoquaux, A. Gramfort, V. Michel, B. Thirion, O. Grisel, M. Blondel, P. Prettenhofer, R. Weiss, V. Dubourg, J. Vanderplas, A. Passos, D. Cournapeau, M. Brucher, M. Perrot, E. Duchesnay, Scikit-learn: machine learning in Python, *J. Mach. Learn. Res.* 12 (2011) 2825–2830.
- [52] GPy, GPy: a Gaussian process framework in python, <http://github.com/SheffieldML/GPy>, since 2012.
- [53] Andrei Paleyes, Mark Pullin, Maren Mahsereci, Neil Lawrence, Javier González, Emulation of physical processes with emukit, in: Second Workshop on Machine Learning and the Physical Sciences, NeurIPS, 2019.
- [54] Martín Abadi, Paul Barham, Jianmin Chen, Zhifeng Chen, Andy Davis, Jeffrey Dean, Matthieu Devin, Sanjay Ghemawat, Geoffrey Irving, Michael Isard, et al., Tensorflow: a system for large-scale machine learning, in: Osdi, Savannah, GA, USA, vol. 16, 2016, pp. 265–283.
- [55] Ilya M. Sobol, Global sensitivity indices for nonlinear mathematical models and their Monte Carlo estimates, *Math. Comput. Simul.* 55 (1–3) (2001) 271–280.
- [56] Jon Herman, Will Usher, SALib: an open-source python library for sensitivity analysis, *J. Open Sour. Softw.* 2 (9) (jan 2017).
- [57] Andrea Saltelli, Making best use of model evaluations to compute sensitivity indices, *Comput. Phys. Commun.* 145 (2) (2002) 280–297.
- [58] Jeremy E. Oakley, Anthony O'Hagan, Probabilistic sensitivity analysis of complex models: a Bayesian approach, *J. R. Stat. Soc., Ser. B, Stat. Methodol.* 66 (3) (2004) 751–769.
- [59] Ralph Gertler, Respiratory mechanics, *Anesth. Clin.* 39 (3) (2021) 415–440.
- [60] Neil R. MacIntyre, Evidence-based guidelines for weaning and discontinuing ventilatory support: a collective task force facilitated by the American college of chest physicians; the American association for respiratory care; and the American college of critical care medicine, *Chest* 120 (6) (2001) S375–S395.
- [61] Elad Gilboa, Yunus Saatçi, John P. Cunningham, Scaling multidimensional inference for structured Gaussian processes, *IEEE Trans. Pattern Anal. Mach. Intell.* 37 (2) (2013) 424–436.
- [62] Francisco Sahli Costabal, Paris Perdikaris, Ellen Kuhl, Daniel E. Hurtado, Multi-fidelity classification using Gaussian processes: accelerating the prediction of large-scale computational models, *Comput. Methods Appl. Mech. Eng.* 357 (December 2019) 112602.
- [63] Francisco Sahli Costabal, Felipe A. Concha, Daniel E. Hurtado, Ellen Kuhl, The importance of mechano-electrical feedback and inertia in cardiac electromechanics, *Comput. Methods Appl. Mech. Eng.* 320 (June 2017) 352–368.
- [64] Mauricio A. Sarabia-Vallejos, Pedro Ayala-Jeria, Daniel E. Hurtado, Three-dimensional whole-organ characterization of the regional alveolar morphology in normal murine lungs, *Front. Physiol.* 12 (755468) (2021) 1–11.
- [65] Cécile Patte, Pierre-Yves Brillet, Catalin Fetita, Jean-François Bernaudin, Thomas Gille, Hilario Nunes, Dominique Chapelle, Martin Genet, Estimation of regional pulmonary compliance in idiopathic pulmonary fibrosis based on personalized lung poromechanical modeling, *J. Biomech. Eng.* 144 (9) (2022) 03.
- [66] Daniel E. Hurtado, Benjamín Erranz, Felipe Lillo, Mauricio Sarabia-Vallejos, Pablo Iturrieta, Felipe Morales, Katherine Blaha, Tania Medina, Franco Diaz, Pablo Cruces, Progression of regional lung strain and heterogeneity in lung injury: assessing the evolution under spontaneous breathing and mechanical ventilation, *Ann. Intensive Care* 10 (1) (August 2020).
- [67] Mauricio A. Alvarez, Neil D. Lawrence, Computationally efficient convolved multiple output Gaussian processes, *J. Mach. Learn. Res.* 12 (2011) 1459–1500.
- [68] Haitao Liu, Jianfei Cai, Yew-Soon Ong, Remarks on multi-output Gaussian process regression, *Knowl.-Based Syst.* 144 (2018) 102–121.
- [69] Taco de Wolff, Alejandro Cuevas, Felipe Tobar Mogptk, The multi-output Gaussian process toolkit, *Neurocomputing* 424 (2021) 49–53.
- [70] Quan Lin, Jiexiang Hu, Qi Zhou, Yuansheng Cheng, Zhen Hu, Ivo Couckuyt, Tom Dhaene, Multi-output Gaussian process prediction for computationally expensive problems with multiple levels of fidelity, *Knowl.-Based Syst.* 227 (2021) 107151.
- [71] George Em Karniadakis, Ioannis G. Kevrekidis, Lu Lu, Paris Perdikaris, Sifan Wang, Liu Yang, Physics-informed machine learning, *Nat. Rev. Phys.* 3 (6) (2021) 422–440.
- [72] Pras Pathmanathan, Suran K. Galappaththige, Jonathan M. Cordeiro, Abouzar Kaboudian, Flavio H. Fenton, Richard A. Gray, Data-driven uncertainty quantification for cardiac electrophysiological models: impact of physiological variability on action potential and spiral wave dynamics, *Front. Physiol.* 11 (vember) (2020) 1–20.
- [73] Felipe Concha, Mauricio Sarabia-Vallejos, Daniel E. Hurtado, Micromechanical model of lung parenchyma hyperelasticity, *J. Mech. Phys. Solids* 112 (2018) 126–144.
- [74] Felipe Concha, Daniel E. Hurtado, Upscaling the poroelastic behavior of the lung parenchyma: a finite-deformation micromechanical model, *J. Mech. Phys. Solids* 145 (2020) 104147.
- [75] Daniel E. Hurtado, Nibaldo Avilés-Rojas, Felipe Concha, Multiscale modeling of lung mechanics: from alveolar microstructure to pulmonary function, *J. Mech. Phys. Solids* 179 (2023) 105364.